Title

Numerical evaluation of image homogeneity, signal-to-noise ratio, and specific absorption rate for human brain imaging at 1.5, 3, 7, 10.5, and 14T in an 8-channel transmit/receive array.

Authors

Cao, Zhipeng

Park, Joshua

Cho, Zang-Hee

et al.

Numerical Evaluation of Image Homogeneity, Signal-to-noise Ratio, and Specific Absorption Rate for Human Brain Imaging at 1.5, 3, 7, 10.5 and 14 Tesla in an 8-channel Transmit/receive Array

Zhipeng Cao[1], **Joshua Park**[2], **Zang-Hee Cho**[2], and **Christopher M. Collins**[3,*]

[1]Department of Bioengineering, The Pennsylvania State University, Hershey, PA, USA

[2]Neuroscience Research Institute, Gachon University of Medicine and Science, South Korea

[3]Department of Radiology, New York University College of Medicine, New York, NY, USA

Abstract

Purpose—Predict trends of SNR and absorbed energy in MRI of brain up to 14T.

Materials and Methods—A human head in an eight-channel transmit/receive coil was simulated with Maxwell and Bloch equations to determine excitation homogeneity with RF shimming, image homogeneity, SNR, and absorbed energy in MRI from 1.5 to 14T considering realistic field distributions and relaxation properties.

Results—RF shimming alone achieved a standard deviation in excitation flip angle less than 10° in mid-brain up to 14T, but produced a small region with low excitation on a lower slice. Current reconstruction methods may produce shading artifacts at 14T. SNR increases with a greater-than-linear rate for GRE sequences having short (2 ms) TE and long TR (approximately 2.3-fold increase from 7T to 14T), but a less-than-linear rate if TE is 10 ms (approximately 1.6-fold increase from 7T to 14T). Depending on the sequence, SNR per square root of imaging time may produce a less-than-linear increase with B_0. Whole-head absorbed energy shows a less-than-quadratic increase with B_0 (1.7-fold increase from 7T to 14T).

Conclusion—Numerical simulations indicate that with proper preparation and precautions, imaging of the human brain at up to 14T could be performed safely with advantages in SNR.

Keywords

high field MRI; FDTD; Bloch simulation; signal-to-noise ratio; RF heating; SAR

Introduction

While it is generally expected that MRI at increasingly high static magnetic (B_0) field strengths will provide a variety of benefits, including improved SNR, for a wide range of applications (1–4), at field strengths much above 1.5T wavelength effects in the RF field

*Address correspondence to: Christopher M. Collins, PhD, 660 First Ave, Fourth Floor, Room 403, New York, NY 10016, c.collins@nyumc.org, (212)263-3322.

distributions begin to complicate performance of MRI and a number of studies have indicated that extrapolating results from lower field systems in this regime will not always provide accurate results (5–10). Currently there are numerous whole-body systems at 7T and a few head-only systems at 9.4T. With a system at 10.5T recently introduced (11), a system at 12T under construction (12), and a head-only system at 14T being planned (13), a prediction of the relative potential performance and safety of imaging the human brain at up to 14T is warranted.

Simulation of electromagnetic fields in MRI has been used to predict or better understand a variety of phenomena in MRI (14). While a few field simulation studies have been published on evaluating SNR at increasing field strengths from 1.5T to 9.4T (5–10), these often utilize simple geometrical approximations of the human tissue structure or single-channel volume coils for transmission and reception. These previous studies typically evaluate the "intrinsic SNR," which takes into consideration RF field effects and expected increase in signal strength with B_0, but not effects of B_0 inhomogeneity or B_0-dependent MR relaxation rates. Also, current MR systems for imaging human subjects at 7T or above are often designed to utilize multichannel receive and transmit coils, and can potentially achieve improved transmit and receive characteristics than single channel birdcage or TEM coils.

With the above limitations in previous studies and recent rapid progress in multichannel transmission and reception techniques, a simulation study solving the Maxwell equations for field distributions and the Bloch Equation for MR signal is presented here with the purpose of evaluating the potential of human brain imaging at up to 14 Tesla with methods used fairly commonly at 7T today. Specifically, this study aims to evaluate trends in excitation homogeneity, image homogeneity, SNR, and absorbed energy with multiple-channel transmission and reception for MR scanners at 1.5, 3, 7, 10.5 and 14 Tesla with consideration of all frequency dependent field distributions, relaxation rates, and imaging parameters.

Materials and Methods

Human Head Model

An anatomically accurate, multi-tissue human head model at 2 mm isometric resolution was created by manual segmentation of photo dataset from the National Library of Medicine's Visible Male Project (10). Proton density, chemical shift, mass density, and T_1 values for many tissues were assigned appropriately with reference to the literature (15–20). Whenever possible, frequency-specific T_2^* values for 1.5, 3, and 7T were collected directly from the literature (16). Based on the reported linear R_2^* relationships, the T_2^* values of gray matter and white matter at 10.5T and 14T were extrapolated, as shown in Table 1. Frequency-dependent T_1 values of cartilage, blood (17), fat (18), CSF (15), white matter and gray matter (19, 20) for 1.5T, 3T, and 7T were also collected and were extrapolated for 10.5T and 14T based on published nonlinear relationships of T_1 with frequency for these tissues (20), as shown in Table 2. For other tissue types, T_1 and T_2^* values at 3T (15–18) were used in all simulations. Only brain tissues, with field-dependent T2 values, were used for the subsequent SNR evaluations. Frequency dependent electric conductivity and magnetic permeability values were also collected for the human model based on values published in

literature (21, 22). In general, tissues are slightly diamagnetic with a relative magnetic susceptibility close to that of water ($\mu_r \approx 0.999991$ ppm) while air is slightly paramagnetic ($\mu_r \approx 1.0000004$).

RF Coil Model

An 8-element coil array was simulated for transmission and reception at all frequencies (Figure 1). The diameter of the coil array is 250 mm. Each element of the array was modeled as a loop with 125 mm in length for each edge, and with 12 current sources on each loop, so that lengths of continuous conductors were approximately 4 cm, or an electrical length of 1/12 the wavelength in air at 600 MHz (14T). The coil is surrounded by a copper shield as shown in Figure 1(c).

Electromagnetic Field Calculations

To calculate RF electromagnetic field distributions, Finite Difference Time Domain (FDTD) simulations (23) were performed. Results included the transmit and receive rotating magnetic fields (B_1^+ and B_1^-, respectively), and transmit and receive electric fields for the human head phantom with the transceive array. All simulations were performed using commercially available software (XFDTD; Remcom Inc.; State College PA, USA). To minimize variability of all aspects except those directly related to field strength, field distributions for each coil were determined with current sources across all gaps in the active coil and all gaps in other coils open. An in-house program based on a published method (22) was used to calculate a realistic static B_0 magnetic field distribution for the human head model.

MRI Simulations

A Bloch-based MRI system simulator developed in-house (24) was used to simulate MR images for this study. A slice-selective 2D gradient recalled echo (GRE) sequence was used in this study to evaluate the signal intensity homogeneity, SNR, specific absorption rate (SAR), and absorbed energy. The sequence was generated with an in-house graphical user interface programmed using MATLAB (The Mathworks; Natick, MA USA), and was input into the Bloch simulator. It was used to separately target two different 6 mm thick transverse slices, one at the center of the coil, and the other 32 mm lower than the center slice (with a larger cross-section to evaluate effects due to more severe B_1 field inhomogeneity). Both slices include air cavities, specifically the frontal sinus on the center slice and the sphenoid sinus in the below-center slice. The details of the GRE sequence varied based on different evaluation goals as described below.

To evaluate the change of image contrast and fundamental RF inhomogeneity effects with field strength, Bloch simulations were performed with quadrature transmission and reception. For this purpose, a single GRE sequence protocol was used for different field strengths: 3 ms TE, 500 ms TR, 30º flip angle, 200 kHz BW, 2 mm slice thickness, 128×128 image resolution, and 256×256 mm^2 FOV.

To evaluate the signal intensity distribution achievable with parallel transmission, the calculated distributions of transmit magnetic field were used to simulate RF shimming. The

RF shimming was performed on each slice independently with a routine programmed in MATLAB (The Mathworks; Natick, MA) to find the optimal magnitude and phase sets of each transmit channel to achieve optimal transmit magnetic field homogeneity. For this purpose, a uniform receive sensitivity was assumed in the simulation for convenience of evaluating transmit inhomogeneities independently from the receive field. A gradient echo sequence with 90º flip angle, 100 kHz BW, 128×128 image resolution, 300×300 mm^2 FOV, 6 mm slice thickness, with TEs inversely proportional to the main field strengths (18.67 ms for 1.5T, 9.33 ms for 3T, 4 ms for 7T, 2.67 ms for 10.5T and 2 ms for 14T), and TR equaling 3 times the value of T_1 of gray matter for each field strength (3585 ms for 1.5T, 4308 ms for 3T, 5331 ms for 7T, 5895 ms for 10.5T and 6333 ms for 14T). To evaluate the ability of a more advanced pulse design to improve upon RF shimming results in the lower slice at 14T, a 5-spoke tailored RF pulse with 8 channel parallel transmission and bipolar slice-selection gradient waveform was designed (31). The available signal intensity (sine of flip angle) after the 5-spoke pulse was compared to that of RF shimming based on Bloch simulations.

To evaluate the signal intensity distribution achievable with parallel reception, fully-sampled array images were simulated with RF shimming for transmission and with the calculated B_1^- distributions as the receive magnetic field distributions. These array images were further processed for the combined approximate uniform-receive-sensitivity image based on the adaptive combination reconstruction method (25, 26).

SNR Quantification

With settings similar to those above, simulations with RF shimming and multichannel reception but with B_0-dependent TRs and two different echo times (2 ms and 10 ms, to evaluate the effect of T_2^* relaxation on SNR) were performed for all field strengths, and the image SNR was evaluated quantitatively. Noise covariance matrices were measured and calculated as on an actual MR system by turning off RF excitation (27). Analytical sum-of-squares SNR expression were used (27) to calculate pixel-by-pixel SNR. Because the absolute SNR level in this study is generally larger than 150, noise bias corrections were not applied. The average SNR value for gray matter and white matter on the target imaging slice were measured for each field strength. To account for the increase of T_1 and scan time with increase of field strengths, the SNR values were further evaluated for SNR efficiency by dividing the square root of the scan time used for each acquisition. The square root relationship with time is chosen because SNR can be alternatively improved by increasing the number of averages, and in this situation SNR is proportional to the square root of the number of averages, or the square root of the total imaging time.

SAR and Absorbed Energy Quantification

To evaluate the EM power deposition of MR scanners with different field strengths, the above GRE sequence with B_0-dependent TRs and transmit RF shimming was used to calculate the time-averaged local SAR for the whole human head phantom. Two types of SAR values were calculated by processing the time-averaged local SAR results output from the Bloch simulator based on the current guidelines by the IEC (28): The head-averaged SAR was calculated by averaging the above time-averaged local SAR in the head, and the

maximum 10-gram SAR was calculated using an in-house program (29) which can achieve accurate result at the tissue boundary. To account for the increase of TR and scan time required to maximize SNR with increase of field strength and T_1, the SAR values were further processed by multiplying the scan time used for each scan to calculate the total absorbed energy.

Results

The signal intensity distributions as a function of field strength with quadrature excitation and reception and with constant TE and TR are shown in Figure 2. As expected, with the increase of B_0, off-resonance effects and inhomogeneity become more notable. This includes chemical shift (lipid in scalp appearing further to the left), and signal loss (especially near the frontal sinus). Also, because of the increased Larmor frequency and decreasing wavelength, regions of low signal due to destructive interference of fields, seen primarily in the temporal lobes at 7T and above, become more focal and move closer together. Finally, primarily because of the lengthening of T_1 with increasing field strength, image contrast becomes more T_1-weighted at increasing field strength when TR is held constant.

The signal intensity distributions with RF shimming for excitation and uniform sensitivity for reception are shown in Figure 3. It is shown that RF shimming alone can achieve excitation homogeneity with flip angle standard deviation less than 10° on a single transverse plane near the center of the cerebrum for high field MRI scanners up to 14T. On a larger cross-section, such as that on a transverse plane passing through the eyes, a small region of low excitation is apparent at 14T. This indicates that RF shimming alone with only 8 channels may not be adequate to achieve homogeneous excitation on all slices at this high field strength. Figure 4 illustrates that with more advanced pulse designs, homogenous excitation can be achieved even on this slice at 14T.

The signal intensity distribution with RF shimming, realistic receive magnetic fields and receive array reconstruction techniques are shown in Figure 5. Compared with Figure 3 (obtained with homogeneous receive fields), it is shown that methods commonly used today to achieve homogeneous receive sensitivity may produce noticeable shading artifacts at 14T.

Trends in SNR in the head from the above simulations are plotted against B_0 field strength in Figure 6. The lines of quasistatic approximations were generated from 1.5T, since at 3T and above wavelength effects become significant in the human brain. It is found that with 2 ms TE and nominally long TR (equal to three times that of gray matter T_1 at each field strength), the SNR has a better-than-linear increase with field strength (Figure 6(a)). Considering the effect of T_2* signal loss, the SNR results with 2 ms TE suggest a better-than-increase of SNR. For example, the ratio of average SNR at 14T to that at 7T in brain is 2.44 on the center slice, and 2.22 on the lower slice. This trend should be similar to what would be expected to predictions of intrinsic SNR, which typically consider RF field effects and B_0 field strength, but not B_0 inhomogeneity or tissue relaxation effects. With TE of 10 ms (commonly used in scanners at 3T and below), the SNR trend becomes less-than-linear with B_0 due to increased T_2* signal loss. For example, the ratio of average SNR at 14T to

that at 7T in brain is 1.73 on the center slice, and 1.47 on the lower slice. The SNR efficiency, in the form of SNR per square root of imaging time, is shown in Figure 6(b). These SNR efficiency trends are similar to the SNR trends, as expected from the fact that T_1 does not increase rapidly with B_0 (Table 2). This accounts for the fact that, due to the lengthening of T_1 with field strength, a longer imaging time may be required to reach a higher SNR.

Trends in absorbed energy in the head from the above simulations are plotted against B_0 field strength in Figure 7. Head-average SAR is shown as a function of field strength in Figure 7(a). The head-average absorbed energy, Figure 7(b), shows a less-than-quadratic relationship with the main magnetic field strength. For example, the ratio of head-average SAR at 14T to that at 7T is only 1.72. This would be the same trend if TR were held constant with field strength and can be regarded as the relationship between intrinsic SAR and field strength if only electromagnetic field effects but not tissue relaxation times or sequence parameters were considered. Maximum local 10-gram SAR and head-average SAR are also given in Table 3, along with the ratios of local 10-gram SAR to head-average SAR.

Discussion

In this study, we evaluated the potential for MR imaging with a fixed multichannel RF coil design for transmission and reception with increasing field strength and Larmor frequency by predicting the trend of performance for MR scanners from 1.5T to 14T. Unlike previous simulation studies with similar goals (5–10), we utilized newer concepts and methods with a multichannel RF coil array, took into consideration expected changes of MR tissue parameters with increasing field strength, and considered realistic effects of B_0 inhomogeneity.

With RF shimming, good excitation homogeneity can be achieved for a gradient echo sequence at up to 14T on a transverse slice through the mid-brain. Although excitation homogeneity on a slice inferior to this shows a significant aberration, pulse designs more advanced than RF shimming should be able to overcome this on a slice-by-slice or whole-brain basis at 14T (30). Excitation homogeneity will be further improved with use of more advanced parallel transmission techniques (31, 32), or if transmit arrays with more channels are utilized.

The shading artifacts from the receive field distributions seen at 14T with multichannel reception are noticeable, mainly due to current limitations of commonly-used methods for characterizing the receive magnetic field distributions and further reconstructing uniform receive sensitivity weighted image from multichannel receive arrays in MR experiments.

It is found in this study that the intrinsic SNR in brain follows a greater-than-linear increase with B_0 field strength (with long TR and short 2 ms TE). Although quasi-static approximations for sample-dominant noise indicate that the longitudinal magnetization vector at thermal equilibrium, the receive magnetic field strength, and the square root of noise power should all increase linearly with the B_0 field strength and thus the intrinsic SNR

should increase proportionally with B_0 (1, 2), our numerical simulations indicate a better-than-linear increase, as predicted and explained previously for a volume coil (9). Further, the simulation results for SNR efficiency with B_0-dependent T_1 show a slightly less-than-linear increase with small TE and a further lower trend at longer TE. This may suggest that, depending on the sequence, 14T MRI would require more accurate B_0 field shimming than lower strength systems to maximize achievable SNR. The increase of T_2* signal loss may also imply stronger susceptibility-weighted contrast.

Because TR was increased proportionally to B_0-dependent T_1 in these simulations, the absorbed energy is proportional to the SAR that would be experienced with a constant TR, or intrinsic SAR. Quasi-static approximations indicate that volume-average absorbed energy should increase roughly with the square of the B_0 field strength (1, 2), but our numerical simulations indicate a much lower rate of increase. It is also seen that the maximum local (10g-average) SAR will exceed the recommended limit in current guidelines for local transmit coils in normal control mode operation before the corresponding limit on head-average SAR (28) is exceeded. This indicates tissue heating due to constructive electric field inference will become more severe with B_0, and advanced local SAR and temperature monitoring methods need to be developed for high field MRI scanners.

While this work presents a number of advances over previous methods to predict trends of achievable SNR at field strengths beyond where experiments can currently be performed, there are a number of limitations. Among these, the T_1 and T_2* values used are estimated or extrapolated from values measured at lower field strengths, and the same coil is used at all field strengths. Recent work indicates that at very high frequencies, optimal current distributions may have non-circulating components, leading to increasing use of dipole antennas under some circumstances in high-field MRI (33, 34). Thus it may be possible to achieve even greater increases in SNR with smaller increases in SAR at high field strength than predicted here. Additionally, in this study only RF shimming was used to improve excitation homogeneity with no consideration of SAR. With more advanced pulse designs, either greater excitation homogeneity, lower SAR, or perhaps both can be achieved.

In summary, a multichannel head-only 14 Tesla MR scanners should be able to achieve adequate transmit field homogeneity for gradient echo imaging with standard RF shimming alone on a transverse slice through the middle of the brain. For homogeneous excitation on lower transverse slices or of the whole brain, more advanced pulses may be required. Imaging in the head at up to 14T can achieve a better-than-linear increase in SNR for short TE. The increase of SNR efficiency, however, is slightly less than linear. For longer TE, both SNR and SNR efficiency would increase at a lower rate with B_0 field strength. Both SNR and SNR efficiency follow a less-than-linear increase with field strength using a longer TE, such that B_0 inhomogeneities result in greater intravoxel dephasing with more T_2* signal loss. The head-average SAR increases at a less-than-quadratic rate with field strength up to 14T. Further development of reconstruction methods to homogenize image intensity would be required for standard anatomic imaging with high field MRI.

Acknowledgments

References

1. Hoult DI, Lauterbur PC. The sensitivity of the zeugmatographic experiment involving human samples. J Magn Reson. 1979; 34:425–433.

2. Edelstein WA, Glover GH, Hardy CJ, Redington RW. The intrinsic signal-to-noise ratio in NMR imaging. Magn Reson Med. 1986; 3:604–618. [PubMed: 3747821]

3. Vaughan JT, Garwood M, Collins CM, et al. 7T vs. 4T: RF Power, Homogeneity, and Signal-to-Noise Comparison in Head Images. Magn Reson Med. 2001; 46:24–30. [PubMed: 11443707]

4. Yacoub E, Duong TD, Van de Moortele P-F, et al. Spin-Echo fMRI in Humans Using High Spatial Resolutions and High Magnetic Fields. Magn Reson Med. 2003; 49:655–664. [PubMed: 12652536]

5. Hoult DI. Sensitivity and Power Deposition in a High-Field Imaging Experiment. J Magn Reson Imaging. 2000; 12:46–67. [PubMed: 10931564]

6. Carlson J. Radiofrequency field propagation in conductive NMR samples. J Magn Reson. 1988; 78:563–73.

7. Ocali O, Atalar E. Ultimate intrinsic signal-to-noise ratio in MRI. Magn Reson Med. 1998; 39:462–73. [PubMed: 9498603]

8. Singerman R, Denison T, Wen H, Balaban R. Simulation of B1Field Distribution and Intrinsic Signal-to-Noise in Cardiac MRI as a Function of Static Magnetic Field. J Magn Reson. 1997; 125:72–83. [PubMed: 9245362]

9. Collins CM, Smith MB. Calculations of B1 distribution, SNR, and SAR for a surface coil adjacent to an anatomically-accurate human body model. Magn Reson Med. 2001; 45:692–9. [PubMed: 11283998]

10. Collins CM, Smith MB. Signal-to-noise ratio and absorbed power as functions of main magnetic field strength, and definition of "90°" RF pulse for the head in the birdcage coil. Magn Reson Med. 2001; 45:684–91. [PubMed: 11283997]

11. Gieseke, T. Medical magnet is on its way. Minnesota Daily; http://www.mndaily.com/news/metro-state/2013/11/12/medical-magnet-its-way [November 12, 2013.]

12. Savage, N. [October 23, 2013.] The World's Most Powerful MRI Takes Shape. IEEE Spectrum. http://spectrum.ieee.org/biomedical/imaging/the-worlds-most-powerful-mri-takes-shape

13. Cho, Z-H. Prospects of 14.0T – feasibility and difficulties. Symposium on Extreme High Field MRI; Seoul. November 5–6, 2009;

14. Collins CM, Wang Z. Calculation of radiofrequency electromagnetic fields and their effects in MRI of human subjects. Magn Reson Med. 2011; 65:1470–1482. [PubMed: 21381106]

15. Duck, F. Physical properties of tissue: a comprehensive reference book. London: Academic Press; 1990.

16. Peters AM, Brookes MJ, Hoogenraad FG, et al. T2* measurements in human brain at 1.5, 3 and 7 T. Magn Reson Imaging. 2007; 25:748–53. [PubMed: 17459640]

17. Stanisz GJ, Odrobina EE, Pun J, et al. T1, T2 relaxation and magnetization transfer in tissue at 3T. Magn Reson Med. 2005; 54:507–12. [PubMed: 16086319]

18. Bazelaire CMJ, de Duhamel GD, Rofsky NM, Alsop DC. MR Imaging Relaxation Times of Abdominal and Pelvic Tissues Measured in Vivo at 3.0 T: Preliminary Results 1. Radiology. 2004; 230:652–9. [PubMed: 14990831]

19. Wright PJ, Mougin OE, Totman JJ, et al. Water proton T 1 measurements in brain tissue at 7, 3, and 1.5T using IR-EPI, IR-TSE, and MPRAGE: results and optimization. Magn Reson Mater Phys Biol Med. 2008; 21:121–30.

20. Diakova G, Korb J-P, Bryant RG. The magnetic field dependence of water T1 in tissues. Magn Reson Med. 2012; 68:272–7. [PubMed: 22144333]

21. Gabriel, C. Compilation of the dielectric properties of body tissues at RF and microwave frequencies. Air Force material command, Brooks Air Force Base; Texas: AL/OE-TR-1996–0037

22. Collins CM, Yang B, Yang QX, Smith MB. Numerical calculations of the static magnetic field in three-dimensional multi-tissue models of the human head. Magn Reson Imaging. 2002; 20:413–24. [PubMed: 12206867]

23. Yee KS. Numerical solution of initial boundary value problems involving Maxwell's equations in isotropic media. IEEE Trans Antennas Propagat. 1966; 14:302–307.

24. Cao Z, Oh S, Sica CT, et al. Bloch-based MRI system simulator considering realistic electromagnetic fields for calculation of signal, noise, and specific absorption rate. Magn Reson Med. 2014 in press. 10.1002/mrm.24907

25. Walsh DO, Gmitro AF, Marcellin MW. Adaptive reconstruction of phased array MR imagery. Magn Reson Med. 2000; 43:682–90. [PubMed: 10800033]

26. Griswold, M.; Walsh, D.; Heidemann, R.; Haase, A.; Jakob, P. The use of adaptive reconstruction for array coil sensitivity mapping and intensity normalization. Proceedings of the 10th Annual Meeting of ISMRM; Honolulu. 2002; (abstract 2410)

27. Kellman P, McVeigh ER. Image reconstruction in SNR units: A general method for SNR measurement. Magn Reson Med. 2005; 54:1439–47. [PubMed: 16261576]

28. International Electrotechnical Commission. International standard, medical equipment—part 2: particular requirements for the safety of magnetic resonance equipment for medical diagnosis, 2nd revision. Geneva: International Electrotechnical Commission; 2002. p. 88

29. Carluccio G, Erricolo D, Oh S, Collins CM. An Approach to Rapid Calculation of Temperature Change in Tissue Using Spatial Filters to Approximate Effects of Thermal Conduction. IEEE Trans Biomedical Engineering. 2013; 60:1735–1741.

30. Collins CM, Wang Z, Mao W, Fang J, Liu W, Smith MB. Array-optimized composite pulse for excellent whole-brain homogeneity in high-field MRI. Magn Reson Med. 2007; 57:470–4. [PubMed: 17326169]

31. Grissom WA, Khalighi M-M, Sacolick LI, Rutt BK, Vogel MW. Small-tip-angle spokes pulse design using interleaved greedy and local optimization methods. Magn Reson Med. 2012; 68:1553–62. [PubMed: 22392822]

32. Cloos MA, Boulant N, Luong M, et al. kT-points: Short three-dimensional tailored RF pulses for flip-angle homogenization over an extended volume. Magn Reson Med. 2012; 67:72–80. [PubMed: 21590724]

33. Lattanzi R, Sodickson K. Ideal current patterns yielding optimal signal-to-noise ratio and specific absorption rate in magnetic resonance imaging: Computational methods and physical insights. Magn Reson Med. 2012; 68:286–304. [PubMed: 22127735]

34. Raaijmakers AJE, Ipek O, Klomp DWJ, et al. Design of a radiative surface coil array element at 7 T: The single-side adapted dipole antenna. Magn Reson Med. 2011; 66:1488–1497. [PubMed: 21630342]
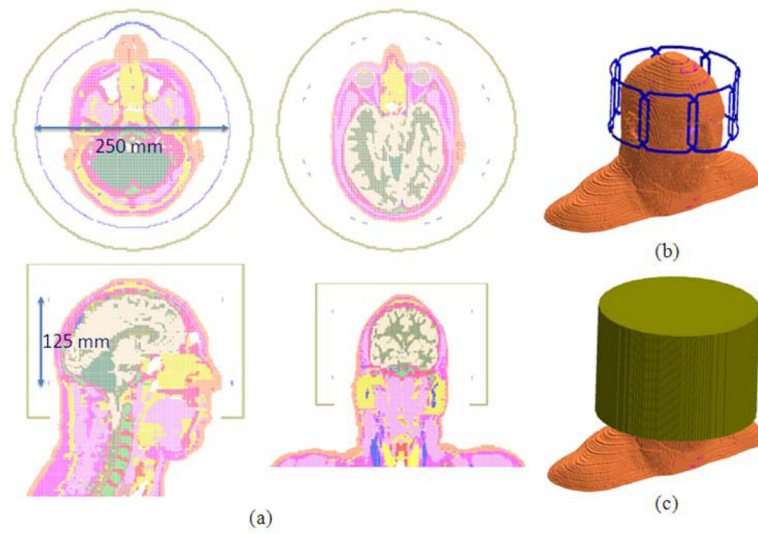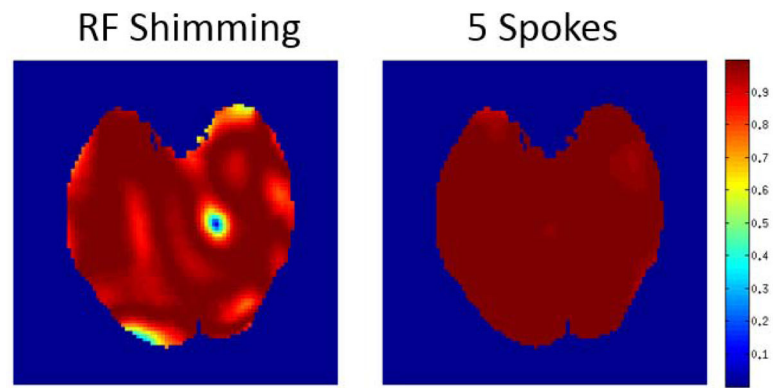
Figure 1.
Schematic diagram of the head, multichannel transmit-receive array, and shield on different cross-sections (a), and 3D renderings of the head in the array only (b), as well as in the array and shield (c).
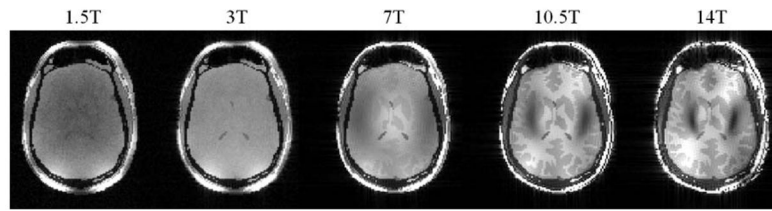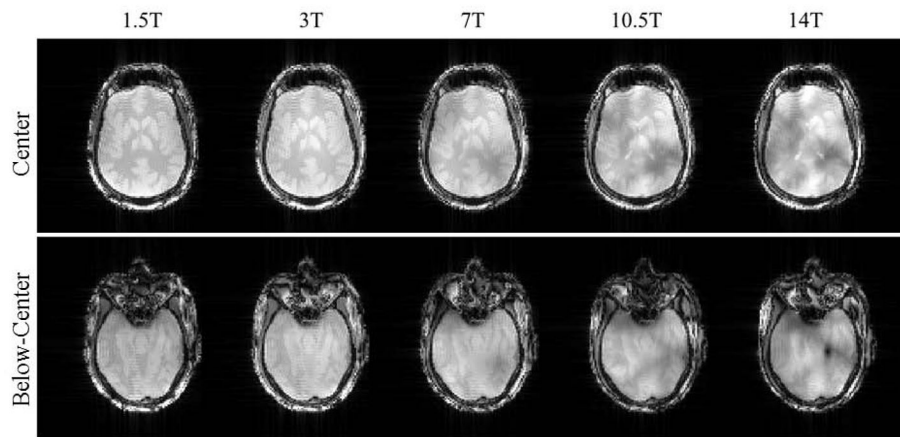
Figure 2.
Simulated MR images with quadrature excitation and reception for different field strengths. Constant TE of 3ms and TR of 500 ms here lead to stronger T_1 weighting at higher field strengths, while decreasing wavelengths decrease both the size of regions of destructive interference and the distance between them.
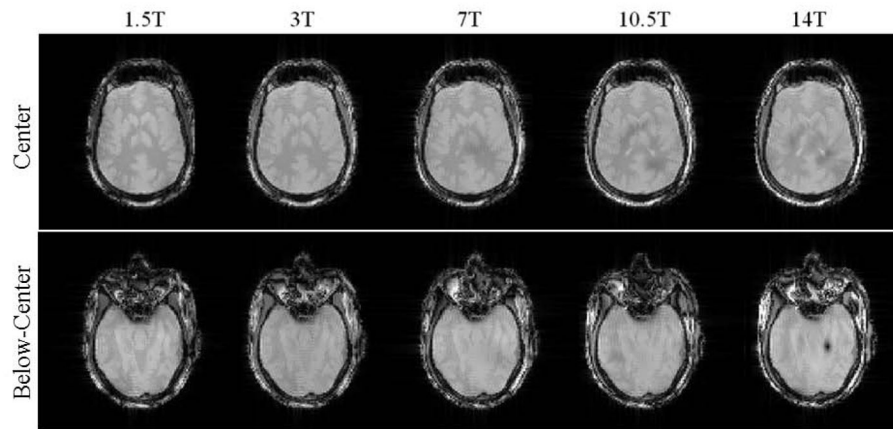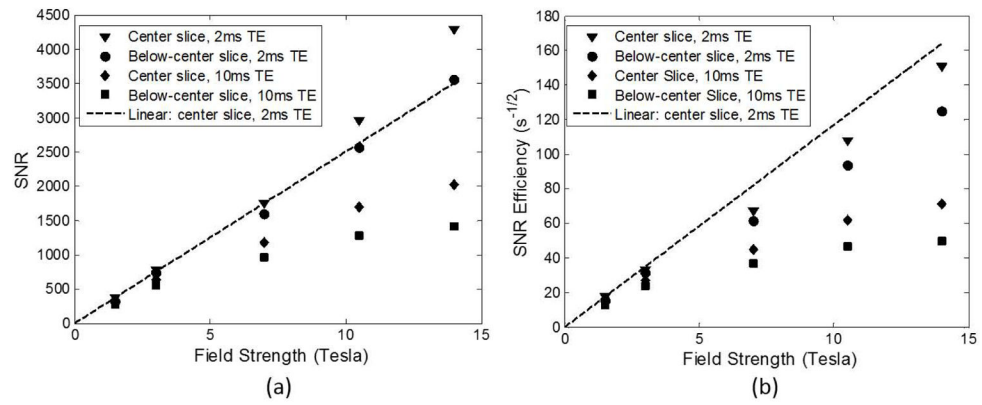
Figure 3.
Simulated MR images with RF shimming for transmission and uniform receive field distribution on the center slice (top) and 32 mm below center (bottom). Here TE is inversely proportional to field strength to minimize B_0 related artifacts and TR is equal to 3 times the T_1 of gray matter to maintain image contrast. At 1.5T, 3T, 7T, 10.5T, and 14T respectively, standard deviations in excitation flip angle of 3.9°, 1.8°, 4.6°, 7.3°, and 9.1° are achieved for the center slice, and of 3.2°, 1.9°, 4.8°, 8.4°, and 9.8° are achieved for the below center slice.

Figure 4.
Comparison of available signal intensity (sine of flip angle) achieved on the lower slice in brain at 14T with RF shimming alone (left) and with a 5-spoke tailored RF pulse (right). Standard deviations in flip angle are 9.8° (left) and 4.1° (right).
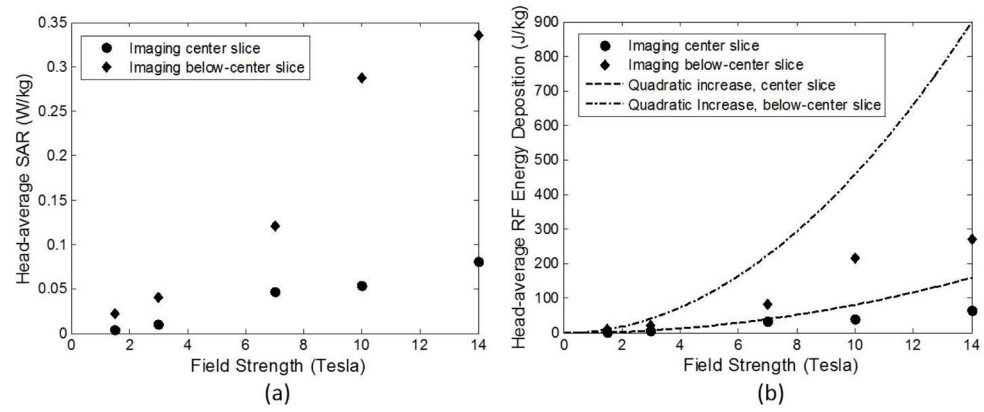
Figure 5.
Simulated MR images with RF shimming for transmission and realistic receive magnetic fields for reception on the center slice (top) and 32 mm below center (bottom). TE and TR vary with field strength as in Figure 3. With the reconstruction method used, shading from the receive field distributions is apparent above 7T.

Figure 6.
SNR with increasing B_0 field strength. SNR (a) and SNR efficiency (b) for 2 ms and 10 ms TE with field-dependent TR equal to 3 times T_1 of gray matter on center and below-center slices. On each plot what would be a linear increase from the value at 1.5T with 2 ms TE are indicated with dotted lines.

Figure 7.
Trends in head-average SAR (a) and absorbed RF energy (b). For SAR, the field-dependent TR is 3 times the value of T_1 of gray matter for each field strength. Thus, the absorbed energy can be compared to the quadratic increase predicted by quasistatic approximations from the values at 1.5T, shown with a dotted line.

Table 1

T_2* Values (in ms) Assigned to Different Tissue Types at Each Field Strength.

Tissue Type	1.5T	3T	7T	10.5T	14T
White Matter	66.2	53.2	26.8	19.2	15
Gray Matter	84	66	33.2	22.2	16

Table 2

T$_1$ Values (in ms) Assigned to Different Tissue Types at Each Field Strength.

Tissue Type	1.5T	3T	7T	10.5T	14T
Cartilage	1024	1168	1552	1888	2224
Blood	1441	1932	3241	4387	5533
Fat	343	382	486	577	668
CSF	4550	4550	4550	4550	4550
White Matter	688	833	1058	1195	1308
Gray Matter	1195	1436	1777	1965	2111

Table 3

Head Average SAR, Maximum 10g Average SAR, and the Ratio of the Two for Different Field Strength with Field-dependent TR. (Ratio for normal control mode in IEC limits is 3.125)

Field Strength (T)	TR (ms)	Imaging Center Slice			Imaging Lower Slice		
		Head-ave SAR (W/kg)	Max 10g SAR (W/kg)	Ratio(max/ave)	Head-ave SAR (W/kg)	Max 10g SAR (W/kg)	Ratio (max/ave)
1.5	3585	0.004	0.0208	5.2	0.0225	0.4239	18.84
3	4308	0.0102	0.05	4.9	0.0405	0.4400	10.86
7	5331	0.0470	0.2498	5.3149	0.1207	1.3466	11.1566
10	5895	0.0539	0.3480	6.4564	0.2877	3.67	12.7563
14	6333	0.0808	0.6480	8.0198	0.3352	3.4817	10.3869